Solving a seismic mystery with a diver's camera: A case of shallow water T-waves in the Persian Gulf

Amir Salaree[1]

Zack Spica[2]

Yihe Huang[3]

Department of Earth and Environmental Sciences
University of Michigan
1100 N University Ave, Ann Arbor, MI 48109

May 14, 2023

for submission to
Geophysical Research Letters

This is a non-peer reviewed preprint.

[1] salaree@umich.edu
[2] zspica@umich.edu
[3] yiheh@umich.edu

Abstract

Sparse offshore coverage of seismic networks has hindered detailed studies of submarine earthquakes and their associated seismic hazard. We present results of our analysis of a diver's recording of acoustic signals from an $M_L = 5.6$ earthquake in the Persian Gulf. We model the signals as a set of several shallow water T phases the frequency and group velocity of which are determined by bathymetry. We show that the audio track from this recording can provide reliable estimates of earthquake location and seismic moment. We also show that the reported shaking in the southern Persian Gulf, > 170 km from the source of this small earthquake could result from T waves traveling through the entire width of the basin. Our results point to rudimentary and affordable underwater microphones similar to those used in the divers' cameras as tools to build efficient, low-cost networks for the study of offshore events and early warning.

Keywords: Seismo-acoustics, Persian Gulf, Divers' Microphones, Seismic Hazard, Early Warning

Plain Language Summary

The lack of offshore seismic stations or the low population of such networks has caused our knowledge of near-shore earthquake sources to be incomplete. To this end, and as a possible tool to study the source of a submarine earthquake, we have analyzed the video recording from a group of divers who have captured the moments during an earthquake in the Persian Gulf region. This earthquake which occurred on the Iranian side of the Persian Gulf was strongly felt along its southern shorelines, more than 170 km from the epicenter. The analysis of this video, which surfaced on social media, points to a set of trapped acoustic signals in the water, or T-waves, in close proximity of the source. We show that such recordings can be reliably used to obtain important information regarding the earthquake source, including its location and magnitude. Besides, we make the case that the reported shaking in Dubai was likely due to the arrival of such high-pitch T- waves from the earthquake. Finally, we propose that cheap microphones existing in standard entertainment cameras can be used to build efficient underwater networks for monitoring small to moderate offshore events.

Key Points:

- We use a diver's camera recording to study an offshore, moderate earthquake in the Persian Gulf.
- A propagation model and simulations of shallow water T-waves are presented.
- Low-cost, entertainment-level subsea hydrophones run by citizen scientists can augment monitoring of offshore events.

1 Introduction

The geographic positioning of the remarkably shallow Persian Gulf with a median depth of 11 m across its 230,000 km^2 span (GEBCO, 2021) in the south of Iran has resulted in the lack of offshore seismic instrumentation (see section S1). This has led to very large azimuthal gaps in southern Iran, especially for offshore, outside-the-network earthquakes. Besides, the sparse lateral coverage of local Iranian seismic networks, such as those operated by the Iranian Seismological Center (IRSC) and the International Institute of Earthquake Engineering and Seismology (IIEES), hinders any detailed studies of the often high-frequency ("snappy"), small-to-moderate events in the region. A classic example was the 25 June 2022 Kish Island earthquake as a part of a seismic cluster along the northern margins of the Persian Gulf. Similarly, studying source structures for larger, more complex earthquake ruptures is practically impossible using global networks due to the attenuation of high frequencies at teleseismic distances (e.g., Chu et al., 2021; Neo et al., 2022). Both issues raise the need for either deployment of new seismic stations, or using other novel, cost-efficient tools to obtain (preferably offshore) seismic data.

1.1 The 25 June 2022 Kish Island Earthquake

A moderate, $M_L = 5.6$ event took place in the Persian Gulf, 27 km east of the Kish Island on 25 June 2022 as reported by the Iranian Seismological Center (IRSC; Fig. 1a) as a part of a seismic sequence in southern Iran (see section S2 and supplementary video SV1). This event was felt in the entire eastern Gulf region including Dubai among other cities along the southern shorelines at a distance of $\sim$ 170 km from the epicenter with numerous reports of strong shaking and displaced furniture (The National, 2022). The earthquake was strongly felt 25 km away in the Kish Island where the shaking caused widespread panic among residents but did not result in any damage (intensity MMI V-VI; Wood & Neumann, 1931); one death and 24 injuries were reported due to the evacuation (Rahborde Moaser,

2022).

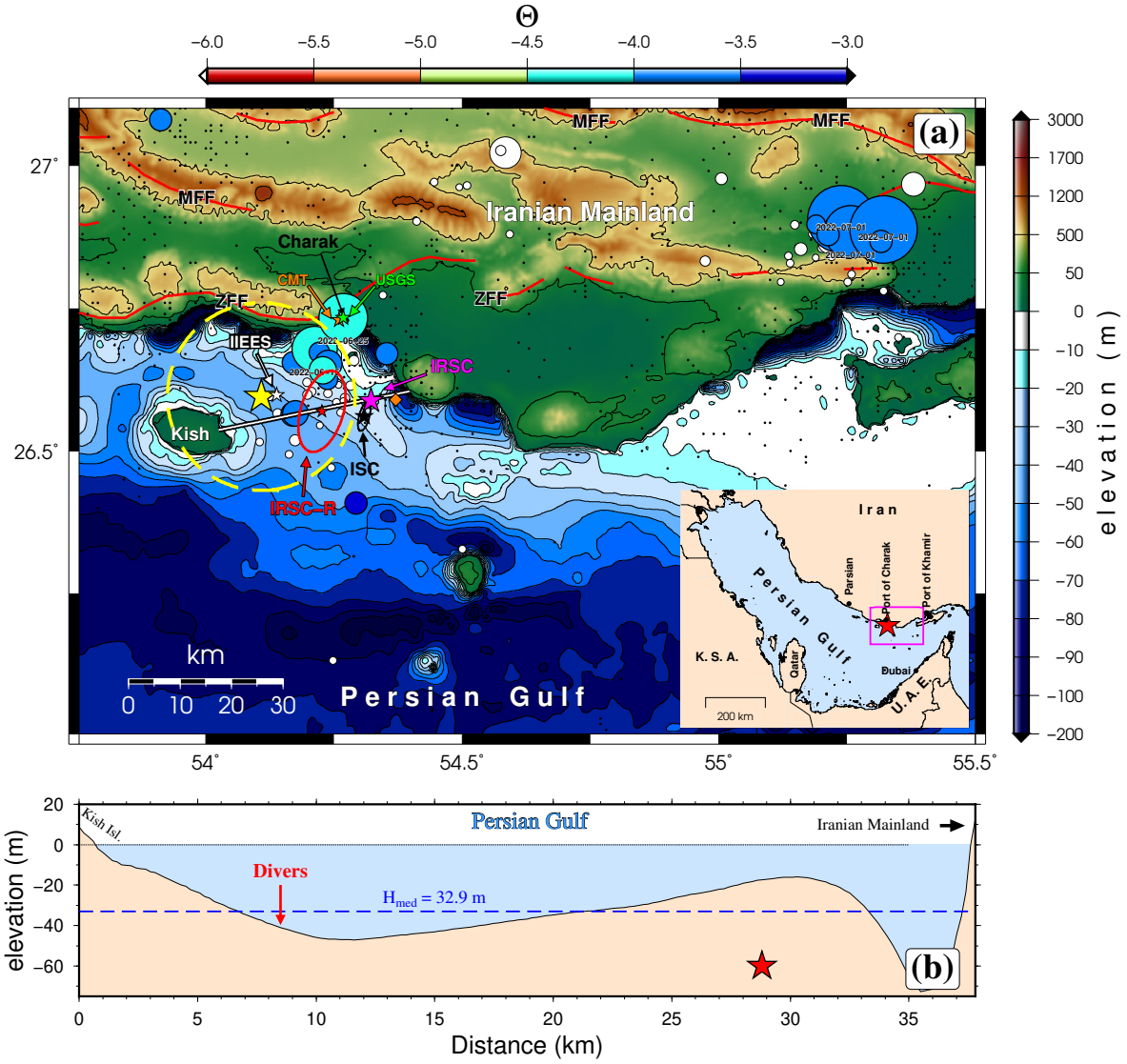

Figure 1: **(a)** Topographic map of the study area. Small, white circle are epicenters of the seismic sequence from the USGS catalog. Larger circles show the locations of $M \geq 4.4$ events for which source slowness values are calculated (colored according to their calculated Θ); corresponding dates are shown. Pink, orange, green and white stars represent epicenters from IRSC, CMT, USGS and IIEES catalogs, respectively. Small red and black stars are relocated IRSC and ISC epicenters shown along with their corresponding uncertainty ellipses. The dashed yellow circle represents the source distance from the divers' position calculated from the analysis of the acoustic signal. Red lines show active fault lines (Hessami et al., 2003). Black dots represent background seismicity from IRSC. The tile map on the bottom right shows the study area in the region. **(b)** Bathymetric cross-section along the white transect line shown in (a). Red star marks the geographic position of the source (i.e., focal depth is exaggerated). The horizontal dashed line depicts the median depth of the Persian Gulf along the transect.

The available CCTV footage from the stores in the Kish Island show $\sim$ 10 s of shaking

(section S3 & supplementary video SV2) from the June 25 event. This duration at a distance of $\Delta = 25$ km from an $M_L = 5.6$ event is consistent with the short ($\sim$ 1.5 s) CMT half-duration of the rupture (Ekström et al., 2012) and the simple, $\sim$ 5 s SCARDEC source time function [Vallée et al., 2011; Vallée, *personal comm.*; see section S4 in supplementary material], as e.g., predicted by Lee et al. (1972). The strong shaking can be attributed to the high- frequency content of the source as illustrated by its anomalously high slowness value of $\Theta = -4.3$ from the algorithm by Newman & Okal (1998) (section S5 in supplementary material). We recall that Θ is calculated using teleseismic body waves as a measure of the radiated energy from earthquake to its seismic moment (typically $-7.0 \lesssim \Theta \lesssim -3.0$ where the low and high bounds represent slow and fast ruptures, respectively).

There is considerable disagreement about the location of this earthquake among reporting agencies with both USGS and CMT placing the epicenter on land close to Charak (green and orange stars in Fig. 1a), and the ISC epicenter located 20 km due south in the Persian Gulf (black star), close to that from the IRSC shown by a pink star in Fig. 1a. The offshore epicenter published by the IIEES, however, is 20 km away from both CMT/USGS and ISC/IRSC epicenters (white star in Fig. 1a). For details, see section S6 in supplementary material.

2 Data: Divers' Recording

A "roaring" audio signal was documented during the earthquake, in a camera recording by divers in Kish who were scuba diving near the northeastern side of the island. The divers' location is depicted by a yellow star in Fig. 1 and a red arrow in Fig. 1b as the bathymetric cross-section along the white transect in Fig. 1a connecting the ISC epicenter to the Kish Island. The video and audio of the distributed recording, included as supplementary video SV3, are sampled at 1502 kb/s and 48 kHz, respectively. The audio contains a long acoustic signal which cannot be directly synced with the earthquake due to the missing

correct timestamps. The time series from the audio and its computed spectrogram are shown in Fig. 2.

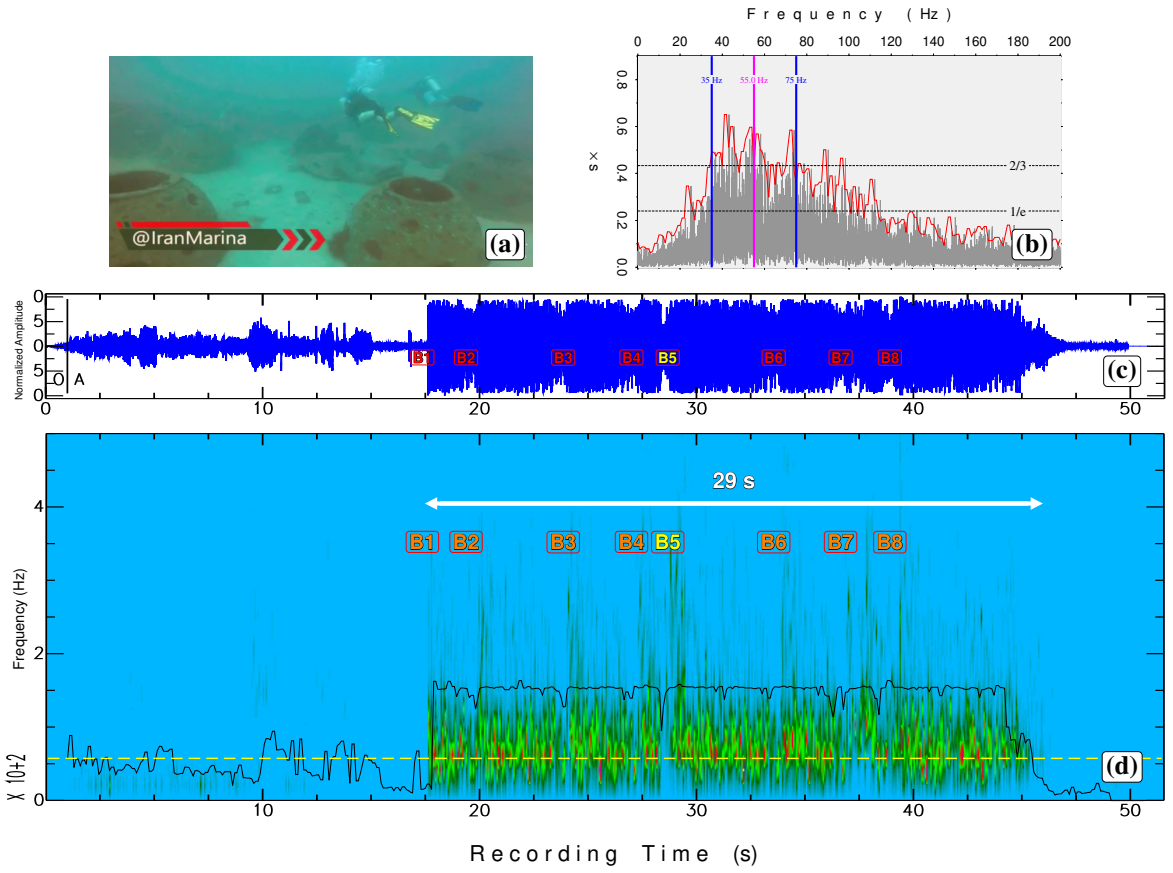

Figure 2: (a) A screenshot of the divers' recording. (b) Fourier transform of the normalized time series from the audio track shown in (c), displayed between 0–200 Hz (gray) along with the computed spectral envelope (red). Vertical blue lines mark an estimated domain of maximum power, i.e., between 35–75 Hz, selected as the frequency range where the power is consistently $\geq \frac{2}{3} P_{\max}$. The pink line shows the mean of the marked range, i.e., 55 Hz. (c) Normalized time series from the audio track of the diver's recording. (d) Spectrogram of the record shown in (c); the double-headed arrow shows the duration of the signal. The numbers in both panels mark the audio booms; the yellow label (B5) depicts the largest, most distinct boom before which the time series intensity falls to $\sim 50\%$ of its normalized envelope. The black curve represents the maximum amplitude envelope for time series scaled to fit the spectrum.

Among the many interesting features of Fig. 2 are: (1) the $\sim$ 29 s long signal, significantly longer than the event's STF and what is expected from the separation of body wave phases in the near-field, (2) the acoustic signal has a dominant frequency of $\sim$ 55 Hz, (3) there are eight distinct *booms*, (4) the recording has a sharp start, but a tapered end; a

property also shared by some of the individual booms, (5) the booms do not occur at fixed time intervals, i.e., they are not periodic, and (6) the fish in the video do not seem to be affected by neither the roaring sound nor the individual booms. Below, we provide a simple model for the acoustic signal while addressing each of these features.

3 Method: Modeling the Recorded Signal as a Trapped Acoustic Phase

Unaffected fish in the divers' video points not to a gravity wave, but an acoustic signal (section S7 in supplementary material; supplementary video SV4). Similarly, the aperiodic nature of the booms in the recording reveals separate acoustic signals rather than overtones (Bloothooft et al., 1992). The entrapment of acoustic signals from active seismic sources has been well-studied in seismic sections acquired via marine surveys from subsurface explorations (Sarrafian, 1956). The near-perfect reflection at the sea-air interface with $R \approx -1$ (Aki & Richards, 2002) and a very small critical angle (near-vertical incident rays) at the sea floor due to the large velocity contrast between sediments and water results in sequences of unwanted reflections in the so-called "singing" exploration records (Backus, 1959). In such cases, reverberations of the acoustic phase, especially in shallow water as frequently documented in the Persian Gulf (Backus, 1959) pollutes target phase arrivals from subsurface strata. The porous sea floor of the Persian Gulf (Tavakoli & Jamalian, 2019) attenuates a significant portion of the high-frequency content of active (i.e., explosive) sources used in marine surveys (Sarrafian, 1956; Cormier, 1982) and thus their acoustic signals are often short-lived. Similarly, the viscoelastic interaction of the porous sediments can result in the lack of total internal reflection at higher frequencies altogether (Stoll & Kan, 1981).

Earthquakes, however, have geometrically larger sources compared to those used in marine surveys (several orders of magnitude), and possess wider, usually red-shifted spectra. This can result in special cases where following consecutive reflections, the significantly less

attenuated signals (due to lower frequency) arrive upon the rock-water boundary at large enough angles and thus subsequent incident angles are super-critical. As a result, the trapped signal can travel long distances with close to zero energy loss. One can show that for a flat sea bed and an incident body wave at angle i_0, the apparent frequency, f and group velocity, v_g are given as (section S8):

$$f = \frac{v_a}{w}\sqrt{1 - \frac{v_a^2}{v_P^2}\frac{\tan^2 i_0}{(1+\tan^2 i_0)}} \qquad , \qquad v_g = v_a\sqrt{1-(v_a/v_P)^2\sin^2 i_0} \tag{1}$$

where v_a, v_P, and w are the acoustic velocity of water, elastic P wave velocity in the sea bed, and depth of the water column. The geometry is increasingly more complex for inclined or more realistic, uneven sea floors, but in these cases one can solve the problem numerically. Such solutions involve propagating a monochromatic ray from the elastic-to-acoustic conversion point toward the receiver, bouncing up and down between the seabed and the free surface. In such cases, the dominant frequency is the inverse weighted integral of reflection intervals; equivalent to the average of point frequencies along the path.

The main assumption in Eq. (1) is that a flat seabed is a good approximation for the Persian Gulf as a remarkably shallow, large basin with an average slope of 0.2% (section S9). According to Eq. (1), the dominant frequency and group velocity of the trapped acoustic phase will remain constant in a flat seabed regime. Using Eq. (1) one can show that for $2.0 \leq V_P \leq 5.0$ km/s, $1.6 \leq V_a \leq 1.7$ km/s (Wright, 1974), $5 \leq w \leq 50$ m, and $0^\circ \leq i_0 \leq 45^\circ$, only a depth range of $29 < w < 38$ m can result in $f = 45 \pm 1$ Hz, i.e., the maximum value from the divers' video (see Figs. 2 and S12). This result is in agreement with documented average depth of ~ 34.6 m from bathymetric data (Fig. 1b; GEBCO, 2021). We note that while the 9 m depth range reflects the uncertainties in the parameters in Eq. (1), it is almost equal to the $\sigma = 9.8$ m standard deviation of the bathymetric profile between source and receiver, or the non-flatness in Fig. 1b. This warrants an investigation of non-flat scenarios.

Numerical experiments for downhill propagation scenarios reveal a gradual increase with depth in group velocity and a decrease in frequency. We attribute this to the increase in incidence angle upon consecutive reflections which causes the wavefield to bounce up and down less frequently while traveling increasingly larger horizontal distances (section S10). In fact, one can analytically show that in the downhill direction, the incidence angle is increased upon each reflection at the seabed by twice the slope angle (e.g., Johnson et al., 1963). This also results in further deviation from the critical angle, hence ensuring efficient, super- critical propagation.

The situation is reversed for the uphill case, where incidence angles decrease by the same amount during each reflection until no further reduction is possible and consequently the propagation direction is flipped. Under such circumstances, a large number of sub-critical reflections may eventually cause the propagation to attenuate and cease unless the wavefield succeeds in turning super-critical again. This depends on both the reflection coefficient and the slope angle while a moderate $30 \lesssim Q \lesssim 60$ (obtained by multiplying successive sub-critical reflection coefficients) will cause reflections to be moderately damped.

4 Simulation: Persian Gulf Trapped Acoustics as Shallow Water T-Waves

The elongated, high frequency (>> 10 Hz) signal in the divers' recording, the spindle-shaped coda of the main envelope, and the individual booms are reminiscent of T-waves. Also similar to T-waves, the long ~ 29 s duration of the acoustic signal (typically expected to have been created by the complex interaction of body waves from the earthquake with the sea floor) is well in excess of predictions from scaling laws (e.g., Geller, 1976). This interval is almost twice as long as what is prescribed by the body wave train duration parameter, i.e., $\tau_{1/3} = 14.7$ s, obtained from teleseismic data (Okal, 2013) (section S11).

In their study of transoceanic T-waves, i.e., seismo-acoustic waves trapped in a low-velocity oceanic layer known as the SOFAR channel (Ewing et al., 1946), Okal & Talandier (1986) showed that the signal duration increases with seismic moment as $M_0^{1/3}$ and is thus linearly proportional to rupture length. In our model, the simple conversion process predicts a direct correlation between the duration of rupture and that of the acoustic wave train. However, as the seismic and acoustic phases will not be well separated in the near-field, the overall duration of the signal may actually correspond to a combination of those from individual seismic phases converted to acoustic waves at (1) both the source and the receiver and (2) along the acoustic path. Fig. 3a shows the computed arrival times of seismic (P and S) and acoustic (T) phases from 5-second long sources (following SCARDEC) at various depths (10-20 km) to receivers at a range of distances (0-50 km) using v_P and v_S velocities for porous limestone (Ross et al., 1986; Tugrul & Zarif, 2000). It is readily seen in Fig. 3a that at a distance of $\sim$ 18 km, i.e., that of the ISC epicenter to the divers' location, P and S wave envelopes will be mixed and the tail of the S-wave packet will overlap with the start of the T phase, hence resulting in a long apparent total duration.

To investigate this issue, we simulate three different acoustic phases from a 10 s long wave train along the bathymetric profile between the ISC epicenter and the divers' location (Fig. 1b) for fully reflective sea surface and sea floor, as shown in Figs. 3b-g. This duration is chosen to mimic a total body wave envelope including both P and S waves arriving at sea bed from a source with an $\sim$ 5 s long STF at a depth of 10 km (see Fig. 3a). This duration is in agreement with the near-field body wave trains recorded by the Iranian strong motion network (section S12; BHRC, 2023). The *abyssal* acoustic phases, i.e., the P and S waves converted to acoustic energy at the receiver, cannot propagate uphill far enough to exit the abyssal plane. The result is the formation of stagnant phases that keep flipping directions and pass the location of divers multiple times until they eventually attenuate and damp out due to sub-critical reflections; a process not taken into account in these simulations (see section 3). However, the direct acoustic phases, i.e., body waves converted to acoustic

energy at the epicenter, henceforth the T phase, successfully crosses the receiver, due to the large incident angles that resulted from having traveled 17 km in the downhill direction. Supplementary video, SV5, shows the simulation results for the three phases over time (see also section S13).

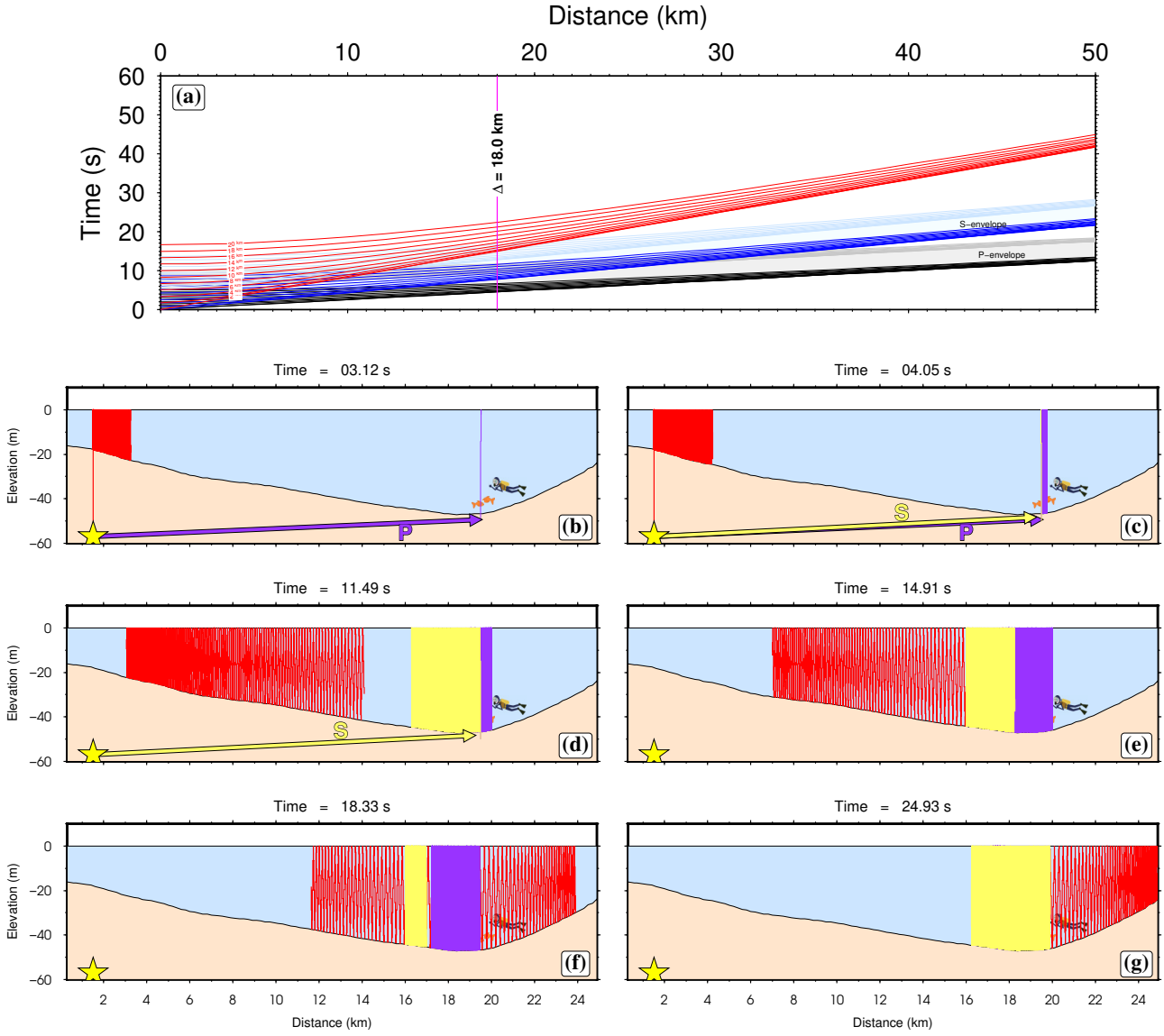

Figure 3: (a) Arrival times of seismic P (black) and S (blue) and acoustic T (red) waves from source to receivers at various distances for sources at 0 to 20 km depths. Shaded gray and blue areas show P and S envelopes for 5 s long sources, respectively. The vertical pink line depicts the approximate distance between the divers' location and the ISC epicenter. (b–g) Bathymetric profile of the Persian Gulf along the transect in Fig. 1 (flipped to place the source on the left), and snapshots of the numerical 2-D ray tracing for the T wave based on our proposed model at **(b)** arrival of direct P, **(c)** arrival of direct S, **(d)** end of P wave train, **(e)** arrival of T wave, **(f)** mixture of all three, and **(g)** end of the T wave train. Purple and yellow line sets are acoustic signals converted from P and S waves ($P \rightarrow T$ and $S \rightarrow T$, respectively) at the location of divers; red lines show the acoustic ray from $P \rightarrow T$ conversion at the epicenter. Location of the divers is also shown. Yellow star depicts the nominal, horizontal location of the hypocenter. Note the exaggerated vertical scale.

Upon considering the stagnant phases, we attribute the booms in the recording (Fig. 2) to the various acoustic arrivals. Based on this assumption, our numerical simulations predict the T phase as the *fifth* acoustic arrival to cross the divers' location. Also, the divers' signal duration, i.e., from the arrival of the abyssal acoustic to the end of the T wave train, is ~ 25 s. Furthermore, the average predicted acoustic frequency and group velocity of the T phase are $f \approx 47$ Hz and $v_g = 1.2$ km/s, respectively.

5 Results and Discussion

5.1 Location Improvement

According to our model and the simulation described in section 4, the first two arrivals in the booms sequence (B1 and B2) are abyssal acoustics from direct P and S waves at the receiver. The difference in their arrival times (~ 2.5 s) and the P and S wave velocities for porous limestone, i.e., $V_P = 5.5$ and $V_S = 3.2$ km/s (Tugrul & Zarif, 2000), result in an epicentral distance of $\Delta = 18.8$ km. Similarly, using the time difference between the P and T arrivals (~ 11.5 s between B1 and B5), and the T phase group velocity from our simulation, i.e., $v_T = 1.2$ km/s, we calculate a distance of $\Delta = 18.2$ km. These values are remarkably consistent (off by only 600 m or $\sim 3\%$), and as shown by the dashed, yellow circle in Fig. 1a, they coincide with the IRSC and ISC epicenters. However, the computed distance is more than 5 km of the published USGS and CMT epicenters (Fig. 1a) which are located on land. As such, the complex seismic-to-acoustic conversion for an on-land earthquake would simply increase the arrival time difference between P and T phases (Johnson et al., 1963) compared to the observed signal.

5.2 Frequency Band

Our model does not foresee any practical limit on the minimum possible frequency of trapped acoustic in the Persian Gulf as a shallow SOFAR channel because frequency is predicted to decrease smoothly with depth down the continental slope. Based on this model, the consecutive reflections will continue with increasing depth until either the low-frequency signal falls below the oceanic microseism threshold (Hilmo & Wilcock, 2020; Janiszewski et al., 2022), or it reaches the global SOFAR channel upon deepening of the continental slope where it will propagate as a compressional T wave (Johnson et al., 1963). While this property limits the largest possible distinguishable magnitude due to scaling laws, acoustic duration is still a reliable discriminant in this regard (e.g., Geller, 1976; Okal, 2008). The total simulated duration ($\sim$ 25 s) of the signal is a combination of abyssal waves and the direct T phase. This is supported by the 50% decrease in the recorded divers' signal just before the arrival of the largest boom, B5, which we attribute to the estimated end time of the abyssal waves via attenuation and the arrival of the T phase, respectively.

On the other hand, the maximum attainable frequency in the shallow SOFAR channel is determined by the acoustic phase velocity as well as the basin's smallest "practical" depth, i.e., the shallowest point which can accommodate the acoustic wavefield. While the latter has been measured for the Persian Gulf (e.g., Wright, 1974), constraining the former is not straightforward mainly due to the complex interactions of acoustic energy with saturated, porous sediments at high frequencies (Stoll & Kan, 1981). Also, shallowing bathymetry will result in the decay of uphill propagation through the attenuation of sub-critical reflections, and this poses a limit on the near-shore haul of shallow water T waves. To avoid such nonlinear effects, we have empirically chosen to truncate our simulations at a depth of $\sim$ 5 m, which is typically at a distance of several meters from the northern Persian Gulf shorelines.

5.3 High Frequency Shaking in the Near- and Far-Field

While the documented near-field strong shaking at the Kish Island (BHRC, 2023) in southern Iran from the 2022 earthquake sequence is likely due to the snappy nature of the sources, the reported long duration of shaking and the multitude of "felt" events by the residents of the Kish Island cannot be explained by traditional, linear propagation of body waves. A potential cause of the prolonged shaking in this regard may have been the local resonance of the isolated island. However, one can show that because of the Kish Island's geological structure (condensed sand and clay with $V_S < 0.5$ km/s; Lee & Tsai, 2008; Ataie-Ashtiani et al., 2013), its dominant natural resonance frequency is very small ($f_{\max} \sim 0.5$ Hz), significantly lower than 1 Hz, i.e., the typical perceived shaking associated with earthquakes (section S14 in supplementary material). Besides, the small relief-to-length ratio of the island (~ 0.003) does not provide a sufficient medium for resonance (supplementary video SV6; SESAME European Research Project, 2004).

Similarly, the accounts of strong shaking and moving of furniture in Dubai are surprising due to the large epicentral distance of $\Delta > 170$ km. The Coulomb stress transfer from an $M_L = 5.6$ event cannot explain any triggered shaking at such a distance. Also, traditional attenuation models for point sources (e.g., Campbell & Bozorgnia, 2003) predict close to no shaking in Dubai, as shown in Figs. 4a & 4b.

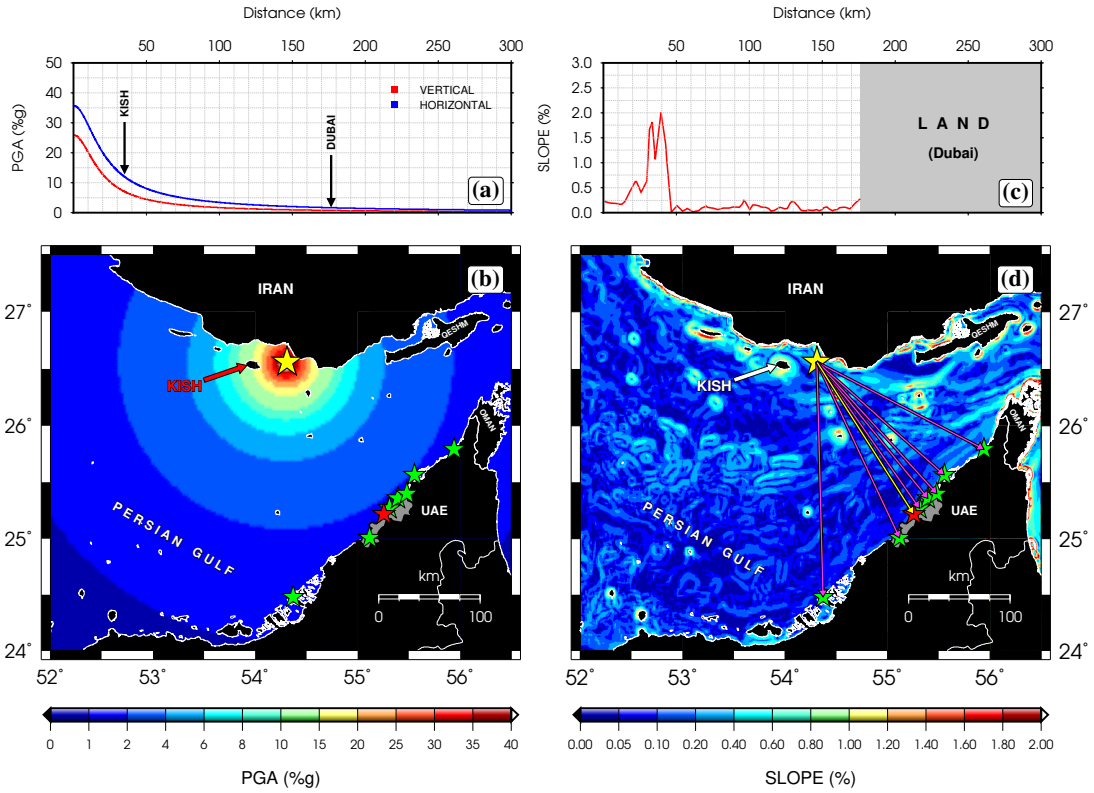

Figure 4: (a) Horizontal and vertical components of PGA as functions of distance for the Kish earthquake computed using attenuation relations from Campbell & Bozorgnia (2003). (b) Geographic distribution of total PGA in the eastern Persian Gulf. Stars represent cities in the UAE; red star shows Dubai. (c) Slope profile (in percents) from the Kish earthquake epicenter to Dubai. (d) Geographic distribution of slope along with examples of acoustic raypaths (pink arrows) from the epicenter to Dubai. The profile in (c) is along the yellow arrow.

In both situations, T waves can shed some light on the properties of shaking. In the Kish Island, where the elastic and acoustic envelopes are not well-separated (see section 4), both the multitude of felt shocks and the apparent long duration of overall shaking may have been due to the belated arrival of T waves after P and S wave trains. Similarly, one can attribute the large observed strong motion at the far side of the Persian Gulf to T waves; T-phase has been successfully used to explain far-field shaking from transoceanic events (Okal, 2008). Analysis of the slope distribution in the eastern Persian Gulf reveals an almost flat seabed with slopes ranging between 0-2% with a median of $\sim 0.1\%$ along the propagation paths from the Kish Island to the Emirates. While it is possible for such slopes to terminate the acoustic path via uphill propagation, we note that the epicenter is not located in the

abyssal plane and the larger slopes appear at least 30 km away. This results in super-critical reflection angles that are large enough to successfully cross the $\sim$ 10 km stretch of slightly steep segments along the path (see Figs. 4c & 4d).

5.4 Implications for Regional Seismic Hazard and Early Warning

Following our proposed propagation model, the apparent multitude of felt back-to-back earthquakes by the residents of Dubai, and the corresponding extreme shaking may be attributed to the arrival of T phase. The modeled T waves are expected to damp quickly upon landfall close to shoreline due to their high-frequency content. However, the resulting attenuation is not sufficient to fully damp out the shaking as the majority of the Emirati infrastructures are distributed along a very narrow ($\sim 5 - 10$ km) stretch of land on the southeastern coast of the Persian Gulf. The far-field shaking in the Emirates raises the need for the inclusion of the corresponding proposed mechanism in future seismic hazard models for the region. It is important to note that the high-frequency shaking is going to have significant implications for the densely populated areas such as Dubai and Abu Dhabi with the majority of the population living in tall buildings (as of 2022, 330 buildings taller than 100 m, with an average height of 184 m, and hosting the tallest building in the world, at 828 m high; CTBUH, 2022).

The late arrival of the T phase in Dubai – compared to its elastic counterparts due to its considerably slower group velocity – from the Iranian earthquakes, however, provides a valuable window of opportunity for early warning. Considering the sparse on-land network coverage in the region and the lack of offshore seismic stations (see sections 1.1 and S1), any estimate of the power of T wave envelopes for future earthquakes in the Persian Gulf will be speculative. Therefore, in order to provide a realistic forecast of the associated hazard, there are two potential avenues ahead. First, it is possible to leverage the dense network of submarine telecommunication cables in the region (section S15 in supplementary material) by deploying repeaters equipped with seismic sensors, hence building a network of the so-

called SMART cables (Rowe et al., 2022). Such arrays have been shown to improve the existing detection threshold of offshore events in several regions of the world (e.g., Salaree et al., 2022). However, while effective, this approach requires long-term planning and is relatively expensive (Matias et al., 2021).

The second, significantly less expensive approach could use a network of cost-effective hydrophones for seismic monitoring, similar to the work of Grangeon & Lesage (2019) in the monitoring of volcanoes. In this contribution, we use the recording from the microphone of a diver's underwater camera to successfully locate an offshore earthquake and evaluate the power of its corresponding acoustic waves by estimating its dominant frequency and duration. Following this idea, one can use a moderate number of well-insulated, low-cost entertainment-grade microphones with appropriate power supplies to serve as a network of hydrophones (Hydrophone Box, or HBox) near regional sources, i.e., in close proximity to Iranian shorelines (section S15 in supplementary material). Connecting these instruments to local facilities for real-time access via radio transmission using buoys serving as antennae is straightforward due to the shallow depth of the Persian Gulf. It is important to note that these hydrophones do not require coupling with the sea bed or a known instrument response. In fact, such microphones often have a flat acoustic response in a broad frequency range, especially at high frequencies. The former feature is important because our approach uses arrival time and duration information (i.e., phase) and thus acoustic amplitude is discarded. Consequently, HBox does not require much rigor during deployment as the only known fixed parameter in this regard are the geographic coordinates of their location.

This method can also be used to map the offshore extent of buried faulting via detection of microseismicity. To this end, similar networks can be readily designed for other regions with comparable morphology and bathymetry, such as the San Francisco region. Other regions where this method can be useful due to large shallow basins and abundant seismicity include but are not limited to the Los Angeles basin off the coast of Santa Monica, Aegean

Sea, the Arafura Sea to the south of Papua New Guinea, and the offshore portion of the Hawai'ian islands.

Acknowledgments

The project significantly benefited from constructive discussions with Robert Holder and Jeroen Ritsema at the University of Michigan. We thank Martin Vallé at Geoscope for providing preliminary SCARDEC source time functions of the 26 June 2022 event. We also thank Saeed Parvin from the IranMarina diving school and Abdolmajid Naderi Beni at the Iranian National Institute for Oceanography and Atmospheric Science (INIOAS) for sharing details of the divers' video. Several figures were created using Generic Mapping Tools (Wessel & Smith, 1998).

Declarations

Funding:

A.S. and Y.H. were supported at the University of Michigan by the National Science Foundation grant PREEVENTS geosciences directorate No. 1663769. A.S. was partially supported by National Science Foundation award EAR2022716.

Conflicts of Interest/Competing Interests:

The authors declare that they do not have any competing interests.

Availability of Data and Material:

Seismic data is available via IRIS. Bathymetry data is available via the General Bathymetric Chart of the Oceans at `https://www.gebco.net/data_and_products/gridded_bathymetry_data/#global`. The divers' recording and other supplementary videos are avail-

able via Deep Blue Data in Salaree et al. (2023) at https://doi.org/10.7302/bbaq-4d43.

Code Availability:

Audio conversion was carried out using SoX available at `https://sox.sourceforge.net`.

References

Aki, K. & Richards, P. G., 2002. *Quantitative Seismology*, University Science Books.

Ataie-Ashtiani, B., Rajabi, M. M., & Ketabchi, H., 2013. Inverse modelling for freshwater lens in small islands: Kish Island, Persian Gulf, *Hydrological processes*, **27**(19), 2759–2773.

Backus, M. M., 1959. Water reverberations - Their nature and elimination, *Geophysics*, **24**(2), 233–261.

BHRC, 2023. Iranian Strong Motion Nework, *Road, Housing & Urban Development Research Center Data Bank*, accessed on 25 Jan 2023.

Bloothooft, G., Bringmann, E., Van Cappellen, M., Van Luipen, J. B., & Thomassen, K. P., 1992. Acoustics and perception of overtone singing, *J Acoust Soc Am*, **92**(4), 1827–1836.

Campbell, K. W. & Bozorgnia, Y., 2003. Updated near-source ground-motion (attenuation) relations for the horizontal and vertical components of peak ground acceleration and acceleration response spectra, *Bulletin of the Seismological Society of America*, **93**(1), 314–331.

Chu, S. X., Tsai, V. C., Trugman, D. T., & Hirth, G., 2021. Fault interactions enhance high-frequency earthquake radiation, *Geophys Res Lett*, **48**(20), e2021GL095271.

Cormier, V. F., 1982. The effect of attenuation on seismic body waves, *B Seismol Soc Am*, **72**(6B), S169–S200.

CTBUH, 2022. The Skyscraper Center, *Council on Tall Buildings and Urban Habitat*, accessed on 24 Jan 2023.

Ekström, G., Nettles, M., & Dziewoński, A., 2012. The global CMT project 2004–2010: Centroid-moment tensors for 13,017 earthquakes, *Physics of the Earth and Planetary Interiors*, **200**, 1–9.

Ewing, M., Woollard, G. P., Vine, A., & Worzel, J. L., 1946. Recent results in submarine geophysics, *Geol Soc Am B*, **57**(10), 909–934.

GEBCO, 2021. Gebco Compilation Group: GEBCO 2021 Grid, *The General Bathymetric Chart of the Oceans*, doi:10.5285/c6612cbe-50b3-0cff-e053-6c86abc09f8f.

Geller, R. J., 1976. Scaling relations for earthquake source parameters and magnitudes, *B Seismol Soc Am*, **66**(5), 1501–1523.

Grangeon, J. & Lesage, P., 2019. A robust, low-cost and well-calibrated infrasound sensor for volcano monitoring, *J Volcanol Geoth Res*, **387**, 106668.

Hessami, K., Jamali, F., & Tabassi, H., 2003. Major active faults of Iran, *IIEES, Tehran*.

Hilmo, R. & Wilcock, W. S., 2020. Physical sources of high-frequency seismic noise on Cascadia Initiative ocean bottom seismometers, *Geochemistry, Geophysics, Geosystems*, **21**(10), e2020GC009085.

Janiszewski, H. A., Eilon, Z., Russell, J., Brunsvik, B., Gaherty, J., Mosher, S., Hawley, W., & Coats, S., 2022. Broad-band ocean bottom seismometer noise properties, *Geophysical Journal International*, **233**(1), 297–315.

Johnson, R. H., Northrop, J., & Eppley, R., 1963. Sources of Pacific T phases, *J Geophys Res*, **68**(14), 4251–4260.

Lee, C.-T. & Tsai, B.-R., 2008. Mapping Vs30 in Taiwan, *TAO: Terrestrial, Atmospheric and Oceanic Sciences*, **19**(6), 6.

Lee, W. H. K., Bennett, R., & Meagher, K., 1972. A method of estimating magnitude of local earthquakes from signal duration, *USGS Open File Report*.

Matias, L., Carrilho, F., Sá, V., Omira, R., Niehus, M., Corela, C., Barros, J., & Omar, Y., 2021. The contribution of submarine optical fiber telecom cables to the monitoring of earthquakes and tsunamis in the NE Atlantic, *Frontiers in Earth Science*, p. 611.

Neo, J. C., Fan, W., Huang, Y., & Dowling, D., 2022. Frequency-difference backprojection of earthquakes, *Geophys J Int*, **231**(3), 2173–2185.

Newman, A. V. & Okal, E. A., 1998. Teleseismic estimates of radiated seismic energy: The E/M_0 discriminant for tsunami earthquakes, *J Geophys Res: Solid Earth*, **103**(B11), 26885–26898.

Okal, E. A., 2008. The generation of T waves by earthquakes, *Adv Geophys*, **49**, 1–65.

Okal, E. A., 2013. From 3-Hz P waves to ${}_0S_2$: No evidence of a slow component to the source of the 2011 Tohoku earthquake, *Pure Appl Geophys*, **170**(6), 963–973.

Okal, E. A. & Talandier, J., 1986. T-wave duration, magnitudes and seismic moment of an earthquake-application to tsunami warning, *J Phys Earth*, **34**(1), 19–42.

Rahborde Moaser, 2022. The M5.6 earthquake shuts down offices in Kish today, *Rahborde Moaser News*, [in Farsi].

Ross, D. A., Uchupi, E., & White, R. S., 1986. The geology of the Persian Gulf - Gulf of Oman region: A synthesis, *Rev Geophys*, **24**(3), 537–556.

Rowe, C. A., Howe, B. M., Fouch, M. J., Angove, M., Aucan, J., Barnes, C. R., Barros, J., Bailiff, N., Becker, N. C., Carrilho, F., Fry, B., Jamelot, A., Janiszewski, H., Kong, L. S. L., Lentz, S., Luther, D. S., Marinaro, G., Matias, L. M., Sakya, A. E., Salaree, A., Thiele, T., Tilmann, F. J., von Hildebrandt-Andrade, C., Wallace, L., Weinstein, S. A., & Wilcock, W., 2022. SMART Cables observing the oceans and Earth, *Mar. Technol. Soc. J.*, **56**(5), 13–25.

Salaree, A., Howe, B. M., Huang, Y., Weinstein, S. A., & Sakya, A. E., 2022. A numerical study of SMART cables potential in marine hazard early warning for the Sumatra and Java regions, *Pure Appl Geophys*, pp. 1–33.

Salaree, A., Spica, Z., & Huang, Y., 2023. Supporting data for solving a seismic

mystery with a diver's camera [data set], *Deep Blue Data - University of Michigan*, https://doi.org/10.7302/bbaq-4d43.

Sarrafian, G. P., 1956. A marine seismic model, *Geophysics*, **21**(2), 320–336.

SESAME European Research Project, 2004. Site EffectS Assessment using AMbient Excitations (SESAME): Guidelines for the implementation of the h/v spectral ratio technique on ambient vibrations measurements, processing and interpretation, *WP12*.

Stoll, R. D. & Kan, T.-K., 1981. Reflection of acoustic waves at a water–sediment interface, *J Acoust Soc Am*, **70**(1), 149–156.

Tavakoli, V. & Jamalian, A., 2019. Porosity evolution in dolomitized Permian-Triassic strata of the Persian Gulf, insights into the porosity origin of dolomite reservoirs, *J Petrol Sci Eng*, **181**, 106191.

The National, 2022. Tremors felt in Dubai after 6.0 magnitude earthquake hits Iran, *United Arab Emirates*.

Tugrul, A. & Zarif, I., 2000. Engineering aspects of limestone weathering in Istanbul, Turkey, *B Eng Geol Environ*, **58**(3), 191–206.

Vallée, M., Charléty, J., Ferreira, A. M., Delouis, B., & Vergoz, J., 2011. SCARDEC: A new technique for the rapid determination of seismic moment magnitude, focal mechanism and source time functions for large earthquakes using body-wave deconvolution, *Geophys J Int*, **184**(1), 338–358.

Wessel, P. & Smith, W. H., 1998. New, improved version of Generic Mapping Tools released, *Eos, Transactions American Geophysical Union*, **79**(47), 579–579.

Wood, H. O. & Neumann, F., 1931. Modified Mercalli Intensity Scale of 1931, *B Seismol Soc Am*, **21**(4), 277–283.

Wright, J. L., 1974. *A hydrographic and acoustic survey of the Persian Gulf*, Naval Postgraduate School.